

Effect of oxygen stoichiometry on the magnetization profiles and negative magnetization in LSMO thin films

Cite as: J. Appl. Phys. **126**, 105301 (2019); <https://doi.org/10.1063/1.5111858>

Submitted: 05 June 2019 . Accepted: 20 August 2019 . Published Online: 09 September 2019

Robbyn Trappen, Alexander J. Grutter , Chih-Yeh Huang, Aubrey Penn, Navid Mottaghi , Saeed Yousefi , Allison Haertter , Shalini Kumari, James LeBeau, Brian J. Kirby , and Mikel B. Holcomb



View Online



Export Citation



CrossMark

ARTICLES YOU MAY BE INTERESTED IN

[Achieving excellent metallic magnet-based absorbents by regulating the eddy current effect](#)
Journal of Applied Physics **126**, 105109 (2019); <https://doi.org/10.1063/1.5109538>

[Insights into the magnetic dead layer in \$\text{La}_{0.7}\text{Sr}_{0.3}\text{MnO}_3\$ thin films from temperature, magnetic field and thickness dependence of their magnetization](#)
AIP Advances **8**, 056319 (2018); <https://doi.org/10.1063/1.5005913>

[Magnetoelasticity of \$\text{Co}_{25}\text{Fe}_{75}\$ thin films](#)

Journal of Applied Physics **126**, 103902 (2019); <https://doi.org/10.1063/1.5116314>

Lock-in Amplifiers
up to 600 MHz



Effect of oxygen stoichiometry on the magnetization profiles and negative magnetization in LSMO thin films

Cite as: J. Appl. Phys. **126**, 105301 (2019); doi: [10.1063/1.5111858](https://doi.org/10.1063/1.5111858)

Submitted: 5 June 2019 · Accepted: 20 August 2019 ·

Published Online: 9 September 2019



Robbyn Trappen,¹ Alexander J. Grutter,² Chih-Yeh Huang,³ Aubrey Penn,⁴ Navid Mottaghi,¹ Saeed Yousefi,¹ Allison Haertter,¹ Shalini Kumari,⁵ James LeBeau,⁴ Brian J. Kirby,² and Mikel B. Holcomb^{1,a)}

AFFILIATIONS

¹Department of Physics and Astronomy, West Virginia University, Morgantown, West Virginia 26506, USA

²NIST Center for Neutron Research, National Institute of Standards and Technology, Gaithersburg, Maryland 20899, USA

³Department of Mechanical and Aerospace Engineering, West Virginia University, Morgantown, West Virginia 26506, USA

⁴Department of Materials Science and Engineering, North Carolina State University, Raleigh, North Carolina 27695, USA

⁵Department of Physics, Pennsylvania State University, 104 Davey Lab, University Park, Pennsylvania 16802, USA

^{a)}Author to whom correspondence should be addressed: mikel.holcomb@mail.wvu.edu

ABSTRACT

The depth-dependent magnetization in thin film oxygen stoichiometric and oxygen-deficient $\text{La}_{0.7}\text{Sr}_{0.3}\text{MnO}_3$ is investigated by using polarized neutron reflectivity and DC bulk magnetometry. The polarized neutron reflectivity results reveal that the stoichiometric sample shows enhanced interfacial magnetization relative to the rest of the film. The oxygen-deficient sample exhibits a reduced average magnetization from the optimized recipe. Both films show regions of suppressed magnetization at the surface regardless of the growth pressure. The oxygen stoichiometric film does not show an interfacial dead layer, whereas the oxygen-deficient film exhibits a dead layer whose thickness changes with temperature. At a low applied field, we observe striking differences in the depth dependence of the magnetic ordering, with the oxygen-deficient film exhibiting exchange spring behavior, while the stoichiometric film shows a constant magnetization direction across the film. These results suggest that the incorporation of oxygen vacancies during growth leads to an accumulation of vacancies at the interface, which is enhanced at higher temperature due to increased oxygen mobility, creating a region of reduced magnetism that couples to the rest of the film. These results offer insight into the complex behavior and role of oxygen vacancies in the magnetism of these systems. Additionally, the study reveals further details of the negative magnetization in $\text{La}_{0.7}\text{Sr}_{0.3}\text{MnO}_3$ reported in previous studies, which are discussed here.

Published under license by AIP Publishing. <https://doi.org/10.1063/1.5111858>

INTRODUCTION

Colossal magnetoresistance manganites have opened the door for a variety of technological applications like magnetic tunnel junctions and magnetic sensors.¹ The widely studied $\text{La}_{0.7}\text{Sr}_{0.3}\text{MnO}_3$ (LSMO) is a particularly appealing candidate due to a large spin polarization and above room temperature ordering temperature.² However, LSMO (and other magnetic oxides) suffer from the degradation of magnetism at small film thicknesses, known as the magnetic dead layer (MDL) problem, which limits the ability to take advantage of these properties for practical

applications. The dead layer is not dead in the strict sense of the word, but rather contains reduced or competing magnetic order.^{3–5} The MDL has been shown to be influenced by multiple factors including interdiffusion,⁶ strain, deviations in stoichiometry,⁷ and others, but the relationship between these factors and how they lead to the formation of the dead layer has not been settled.

Additional insight into the properties of the MDL may be found by carefully controlling the measurement conditions. As was presented by Mottaghi *et al.*, stoichiometric LSMO's

magnetization curve resembles that of a typical ferromagnet when measured under standard field-cooled, high measuring field conditions, while different behavior emerges under zero field cooled (ZFC) and low measuring field conditions including nanoparticlelike blocking behavior as well as negative magnetization at low temperatures.^{8,9} These results indicate that the magnetic ordering in this material is more complex than has been typically reported.

Oxygen vacancies (OVs) are one factor that can substantially affect the properties of the dead layer and the magnetic ordering in thin films. While OVs are known to degrade the magnetic properties of LSMO by disrupting the double exchange interaction,^{10–12} exactly how OVs alter the magnetism throughout the material remains unknown as OVs in general can be difficult to detect, particularly in dilute levels below a few percent. Additionally, the effect of OVs on the magnetization profile and the magnetic dead layer of LSMO thin films has not been established. Polarized neutron reflectivity (PNR) provides one method to measure the effects of the OVs as their presence can modify the scattering length density (SLD), typically by lowering it in the oxygen-deficient region and also by decreasing the magnetization.^{13,14} Here, we present the depth-dependent magnetization of two LSMO thin films grown under oxygen-rich and oxygen-deficient conditions. We show that while oxygen defects are seen to decrease the magnetization when the films are measured under typical conditions, their effect on the magnetic ordering in LSMO becomes more apparent when measured under ZFC/low-field conditions.

METHODS

To study the effect of OVs on the depth-dependent magnetic properties of LSMO, oxygen stoichiometric and deficient films were grown by pulsed laser deposition at a substrate temperature of 750 °C with a laser fluence of 1.3 J cm⁻². Growth pressures were 100 mTorr (1 mTorr = 0.13 Pa) for the oxygen stoichiometric sample and 10 mTorr for the oxygen-deficient sample. To prevent oxygen loss,¹⁵ the oxygen pressure for the oxygen optimized sample was increased to 450 mTorr after growth and during cooling. Films were grown on TiO₂ terminated SrTiO₃ (STO) substrates using a two-step annealing process with a DI water treatment.¹⁶ Step-terrace morphology was observed for the substrates *via* atomic force microscopy (AFM), which is consistent with ideal conditions for layer by layer growth.¹⁵ Phase lag imaging (see Fig. S1 in the [supplementary material](#)) indicated an approximately constant contrast, indicating that single termination was achieved. The reflection high energy electron diffraction (RHEED) pattern for the bare STO (100) direction is shown in Fig. 1. The single bright spot¹⁵ provides additional verification of the substrate TiO₂ termination. The streaky RHEED pattern shown in Fig. 1(b) indicates a smooth film surface as opposed to the spotty streaks seen in Fig. 1(c) for the films grown in lower oxygen pressure. This difference in roughness observed by the RHEED patterns is supported by AFM measurements [Figs. 1(e) and 1(f)], which yield root-mean-square roughnesses of 0.23 and 0.34 nm, respectively.

X-ray reflectivity (XRR) measurements were performed with a Bruker D8 Discover XRD system. Data were fit using GenX software.¹⁷ Fitted parameters consisted of substrate roughness and film

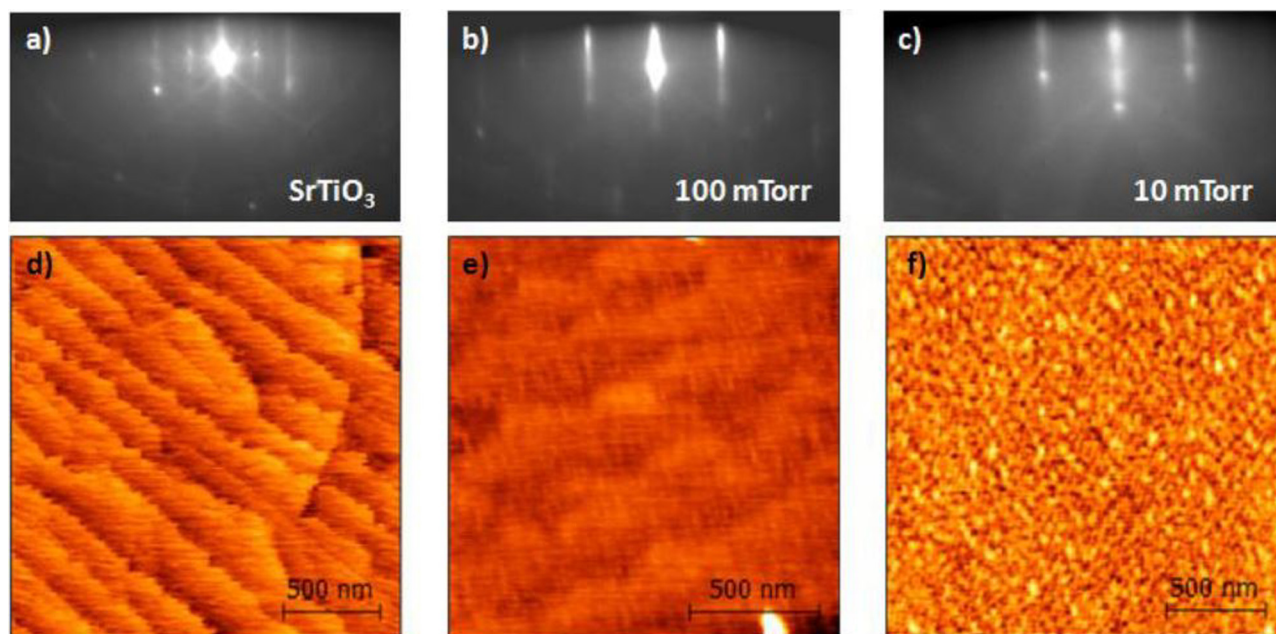


FIG. 1. RHEED pattern of (a) STO substrate, (b) oxygen stoichiometric and (c) oxygen-deficient LSMO film after deposition. (d)–(f) Corresponding AFM images are shown below each RHEED pattern. The RMS roughnesses for images (e) and (f) are 0.23 nm and 0.34 nm, respectively.

thickness and roughness (an intensity scale factor and 2θ offset were also included). Fits along with the corresponding film thickness are displayed in Fig. 2. The two samples were well described by a slab of constant scattering length density (SLD). The fitted sample roughnesses are 0.65 nm and 0.72 nm for the 100 mTorr and 10 mTorr grown samples, respectively, which are slightly higher than those of AFM possibly due to the larger measurement area of 0.1 mm for XRR compared to that of AFM (and, therefore, a greater sensitivity to long-range disorder—a similar scenario is discussed in the modeling of the neutron reflectivity later on). Sample thicknesses were determined to be 17.0 nm and 16.5 nm, respectively. Thus, the thicknesses are close enough to compare the magnetic properties of the films based solely on changing oxygen content.

In order to verify the interface quality of both samples, transmission electron microscopy measurements were performed. Sample preparation details are reported in Ref. 18. Both samples were found to show sharp interfaces as supported by the fitted interfacial roughnesses of 0.34 nm and 0.30 nm determined by XRR (for the 10 mTorr and 100 mTorr sample, respectively). TEM images can be found in the [supplementary material](#), Fig. S2.

To gain insight into the average magnetic properties of the films, magnetic hysteresis measurements were conducted using a Quantum Design PPMS in vibrating sample magnetometry (VSM) mode. Measurements were taken at 5 K after cooling in a 0.1 T magnetic field applied along the STO(100) axes. The diamagnetic contribution was removed by fitting the high field regions (between 0.3 and 0.4 T) to a linear function, which was then subtracted from the whole data set. Afterward, the curves were normalized to the film volume.

PNR measurements were performed using the Polarized Beam Reflectometer (PBR) beamline at the NIST Center for Neutron Research. PNR provides sensitivity to thin film and multilayer depth profiles of the nuclear composition, and vector magnetization, averaged in-plane. Samples were mounted with the STO (100) crystal axis parallel to the field direction. For each sample, data

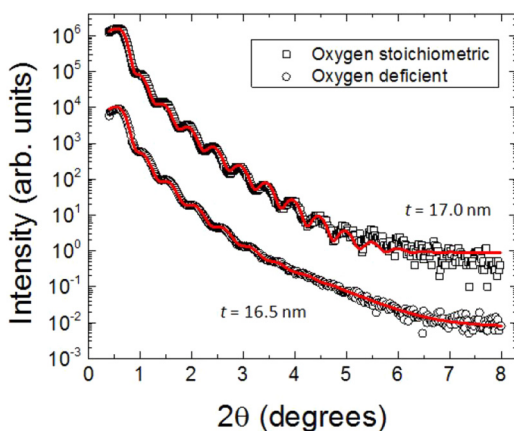


FIG. 2. XRR data (open points) and fits (solid lines) from GenX.

were first taken at 5 K in ZFC conditions, then the field was increased to 700 mT and subsequent scans were taken during warming. As previous measurements have indicated that the magnetism in LSMO is very sensitive to the measurement conditions, the field condition during measurement was carefully controlled. To accomplish this, the samples were cooled down from room temperature to 5 K in as close to the zero field as could be achieved with the experimental setup (a little over $100 \mu\text{T}$ as measured by a Hall probe between the magnet poles), after which the in-plane applied field was increased to 2 mT for the first measurement, then to 700 mT for the subsequent measurements. PNR measurements are shown in Fig. 3 as a function of the out-of-plane momentum transfer q_z (note that the data taken in 2 mT have been shifted for easier comparison to the data taken in 700 mT). The data have been corrected for background, imperfect beam polarization, and beam footprint. Unless otherwise noted, the error bars and uncertainties represent a range of ± 1 standard deviation. The PNR intensity is shown as the nonspin-flip reflectivities R^{++} and R^{--} , meaning that an incident spin up/down neutron is reflected without changing its spin state. Also shown are the spin-flip reflectivities R^{+-} and R^{-+} , where the neutron changes spin state due to the interaction with a magnetization component perpendicular to the applied field,¹⁹ which induces a spin transition. Thus, the nonspin-flip scattering cross sections are sensitive to the depth profile of the nuclear scattering length density and the magnetization along the applied in-plane field, while the spin-flip scattering is sensitive to the depth profile of the perpendicular magnetization component.

The PNR data were fit using the Refl1D software developed at NIST.²⁰ The software utilizes a global search algorithm based on Markov Chain Monte Carlo sampling (the DREAM algorithm²¹) and is very robust against becoming trapped in local minima. The 2 mT and 700 mT data were simultaneously fit for each sample allowing only the magnetization angles (defined as the angle

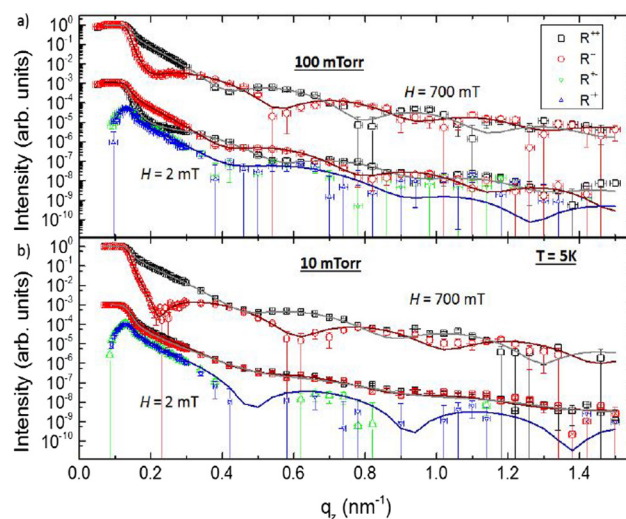


FIG. 3. PNR curves (data points) and fits (solid lines) for the (a) oxygen stoichiometric and (b) oxygen-deficient LSMO films.

between the magnetization and the applied field) and magnetic SLDs to vary between field states; other fit parameters such as density, roughness, and thickness were fixed to be the same for both field states. For the 700 mT fits, the magnetization angle was fixed to be parallel to the applied field. Fit results are shown in Fig. 3 and indicate a good agreement with the data.

RESULTS AND DISCUSSION

The structural and magnetic depth profiles extracted from fitting the PNR data from the stoichiometric and oxygen-deficient samples are shown in Figs. 4(a) and 4(b), respectively. Here, the nuclear SLD profile is representative of changes in the density of nuclei in the material (i.e., the material density), while the magnetic SLD corresponds to the magnitude of the in-plane magnetization. The magnetic angle is defined as the direction of the in-plane magnetization component with respect to the field axis [an example is shown in the inset of Fig. 4(a)—note that for the larger measuring field of 700 mT, the magnetization is parallel to the field axis].

We first examine the reflectivity and depth profiles of the oxygen stoichiometric sample at 700 mT. The oxygen stoichiometric reflectivities were fit to a two-slab model; as shown in the supplementary material (Fig. S3), a one layer model was insufficient to fit the data (note that the model also included the possibility of dead regions at the top and bottom of the slabs with adjustable thicknesses as parameters). The profile for the oxygen stoichiometric sample is consistent with the work of Guo *et al.*²² who report an enhanced interfacial and suppressed surface magnetization similar to the profile shown in Fig. 4(a). The fits indicate that there is no interfacial MDL in this sample. Note that the interface roughness is higher than the atomically flat surfaces as measured by

AFM, with a value of 0.7 nm obtained from the fits. This difference is likely due to surface rumpling of the STO after undergoing the cubic-to-tetragonal structural transition below 105 K,^{23,24} which is well known to cause buckling of the substrate surface but may also be due to the fact that the neutron beam illuminates the entire sample and, therefore, the measurement probes a larger area and is more sensitive to long-range roughness and nonuniformity than AFM, which probes only small areas.

The magnetization is suppressed near the film surface, with a dead layer thickness on the order of 1 nm. This magnetic dead region at the surface is likely responsible for the decrease in phonon-assisted spin-lattice recombination reported in another work, where the effect becomes more significant as the film thickness decreases and the surface contributes more.²⁵ While this could possibly be attributed to an insufficient postgrowth cooldown pressure (450 mTorr for our samples), the magnetization profiles of Guo *et al.* also show a diminished surface magnetism even after annealing in 1 atm of oxygen after growth. This may suggest one of two scenarios: either the origin of the surface MDL is not solely influenced by oxygen defects or that postannealing is not sufficient to recover all of the oxygen lost during growth. The latter is supported by the work of Li *et al.*, who found that films grown in 195 mTorr showed a larger magnetization than those grown in 7.5 mTorr, but which were also postannealed to recover the oxygen content.⁷ Some reports also suggest the possibility of Sr segregation at the surface of the films,^{26,27} although the relatively smooth surfaces of our films shown by AFM suggests that this effect is likely very weak if it is present. Note that our profile also contrasts with those obtained by several other groups,^{28,29} which show both suppressed surface and interface magnetization. As pointed out in Ref. 22, these results seem to indicate that the existence of the

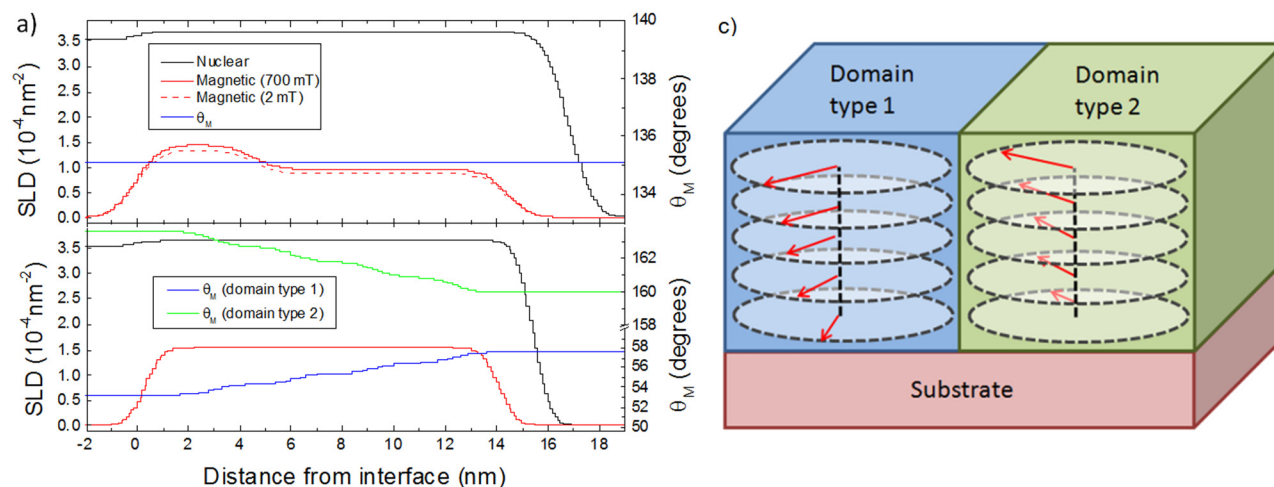


FIG. 4. Nuclear and magnetic SLD profiles (black and red lines, respectively) for (a) oxygen stoichiometric and (b) oxygen-deficient LSMO films. The magnetization angle θ_M is shown on the right axis in (a) and (b) for the 2 mT measuring fields (note that for the 700 mT measurements, θ_M is parallel to the field). The inset in (a) shows the relation between the magnetization angle and the field axis for the optimized sample. (c) Cartoon of the two domain types used in the exchange spring model for the oxygen-deficient sample. The signal is modeled as an incoherent sum of the scattering from the two domain types. The dashed lines in the plane of the film indicate the field axis. The differences in the spin angles between the layers are exaggerated for clarity.

interfacial dead layer is strongly influenced by film growth conditions and can possibly be eliminated by control of the appropriate growth parameters.

Having established the magnetic profile of the stoichiometric sample under typical measurement conditions with a large magnetic field, we now wish to better understand the nature of the negative magnetization observed in the low measuring field in previous works.^{8,9} The magnetization profile of the stoichiometric sample obtained from the fits is shown in Fig. 4(a) as a dashed line. The right axis shows the magnetization angle as a function of depth (for the low-field measurement only). The magnetic SLD obtained from fitting the data from the 2 mT measurement is slightly lower than that of the 700 mT measurement. A slight reduction in magnetization may indicate either spin canting or the formation of some antiparallel domains. However, the extremely small observed difference in magnetic SLD indicates that any such effect is nearly negligible. It is worth noting that the two curves are nearly within error of each other, so this effect is small.

As shown in Fig. 3(a), the position of the spin up and spin down reflectivity curves has switched between measuring fields, indicating a sign change in the magnetization. In addition, the films have a substantial spin-flip reflectivity, which was discussed in the Methods section is indicative of a magnetization component perpendicular to the applied field. The fits suggest that the magnetization angle is constant with depth, rather than originating at the surface or interface. The sign reversal of the magnetization is consistent with our earlier reports^{8,9} and those in Ref. 30. Magnetization sign reversal in LSMO has also been noted by Lee *et al.* in XMCD measurements, although the effect was observed after removal of an applied field rather than after ZFC magnetization measurements.^{31,32}

The fits indicate that the magnetization lies approximately 135° away from the field parallel direction. As the resultant angle is influenced by the balance between the magnitude of the splitting in the $++/-$ reflectivity and the magnitude of the $+/-+$ reflectivity, the model should be quite sensitive to the angle. This value of the magnetization angle may be a result of changes in the magnetic anisotropy of LSMO when it is grown on substrates with the step-terrace morphology. In a study by Mathews *et al.*, the easy axis of thin film LSMO was found to correspond to the [110] direction of STO, i.e., along the terrace step direction.³³ The results were temperature dependent, showing twofold symmetry at room temperature (with the easy axis perpendicular to the step direction and hard axis parallel), but fourfold symmetry at low temperature (with easy axes corresponding to both parallel and perpendicular to the terrace step direction). The angle obtained here from the spin-flip reflectivity is very close to the STO [110] direction. Zero-field cooling the film would allow the magnetization to lie along any of the equivalent STO[110] directions rather than the direction applied field, and only after increasing the field to 700 mT would the spins align with the field. Therefore, it is likely that the direction of the spins observed in our measurements is influenced by the step edges.

While the change in magnetic anisotropy due to the substrate likely plays a role in the magnetization angle observed in the experiment, it does not say anything about the magnetization reversal itself. If any of the film diagonals were equivalent, it would be expected that the ZFC magnetization would be close to zero rather

than the large negative value that we observe. While the exact mechanism responsible is still under investigation, several possibilities have been suggested in the literature. The study in Ref. 30 provides TEM data that show an interdiffusion from the substrate into the film over a distance of 1–2 u.c. (a layer this thin would likely not be detectable by our PNR measurements due to limits of the q range surveyed), which could alter the interfacial magnetism and change its coupling to the rest of the film. Similarly, Refs. 31 and 32 show a thickness dependence to the gradual magnetization reversal after application of an applied field. An alternative explanation has been recently proposed by Mottaghi *et al.* in Refs. 8 and 9, where it was suggested that a superparamagnetic phase had formed in the films which could negatively couple to the ferromagnetic phase; a similar behavior has been noted in LSMO nanoparticles.³⁴ While the origins of the magnetization reversal in LSMO thin films are still unknown, the above studies all seem to point to a complex magnetic ordering in LSMO beyond single phase ferromagnetism, which may involve the interaction of multiple magnetic phases.

Having studied the behavior of the magnetization of the stoichiometric film, we next explore the role of oxygen vacancies on the magnetic profile. Fitted results for the oxygen-deficient sample are shown in Fig. 4(b). The 700 mT measurement of the oxygen-deficient sample was well described by a one-slab model. The fit of this data shows a constant magnetization profile within the bulk of the material with depressed magnetism at the surface, contrasting that of the stoichiometric sample. However, the low-field data for the oxygen-deficient sample was not well fit by such a model, even after including more layers (see in the [supplementary material](#)). We see from Fig. 3(b) that the difference in the nonspin-flip reflectivity is quite small, suggesting that the in-plane magnetization is close to zero. However, attempting to fit the data with a model reflecting a small magnetization resulted in a very poor fit. As discussed in Ref. 35, an assumption in the modeling used for the stoichiometric sample is that the variation of the in-plane magnetic features is small enough that a measurement essentially reflects an average of the magnetic depth profile over the projection of the neutron wave packet onto the sample surface. However, this assumption is no longer valid if, for example, the domain sizes are comparable to or in excess of the coherence length. In this case, it is necessary to model the PNR as an incoherent sum of scattering from multiple distinct depth profiles.

Two alternative models were examined: (1) a horizontal domain model, where the in-plane magnetization breaks up into domains oriented parallel, antiparallel, and perpendicular to the applied field, as well as nonmagnetic regions and (2) a vertical domain model, where the material exhibits an exchange spring type magnetic ordering³⁶ with the spins rotating across the length of the sample. Here, only two types of domains were considered, with oppositely oriented spin spirals. As shown in Fig. S3 in the [supplementary material](#), both types of fits describe the data equally well. Note that for the exchange spring model, the change in the magnetic angle with depth is small—only a few degrees. We attempted to model the system as a single magnetic spiral, which did not result in a good fit (also shown in Fig. S3).

As magnetic hysteresis loops are sensitive to the domain structure of the films,^{36,37} hysteresis curves were measured to distinguish between the two possibilities. Figure 5(a) shows the hysteresis

curves for the two LSMO films taken at 5 K. As expected from the incorporation of oxygen vacancies, the saturation magnetization for the oxygen-deficient sample is lower than that of the oxygen stoichiometric sample. The curve for stoichiometric sample shows a behavior typical of a ferromagnet and that of LSMO films reported in the literature.¹⁵ However, the curve for the oxygen-deficient sample shows a two-component behavior. Such a behavior has been observed in exchange spring systems and is indicative of two regions of different coercivity^{36,38,39} and has been previously observed in LSMO as well,²⁸ although the underlying physical mechanism was not established. This two-component behavior of the hysteresis loop would seem to indicate that the exchange spring model [Fig. 4(c)] correctly captures the magnetic profile as opposed to the multidomain model (which would be a single-component hysteresis loop, with a low value of loop squareness, i.e., low ratio of remnance to saturation^{40,41}).

We note here that the magnetic SLD (proportional to the magnetization) reported in Fig. 4(b) for the low pressure grown sample appears to be larger than that of the high pressure grown sample in Fig. 4(a), in apparent contrast to the above VSM results. This is due to the presence of a large non-FM magnetic signal in the 10 mTorr sample not present in the 100 mTorr film; this contribution is usually subtracted off in VSM but not in PNR. This is a subtle point and is discussed further in the [supplementary material](#), Sec. 5.

The magnetization profile for the exchange spring model is presented in Fig. 4(b). Note that since the reflectivity must be modeled as an incoherent sum of contributions from different domains, the magnetic SLD shown in Fig. 4(b) corresponds to the depth-dependent magnetization, independent of orientation. The total reflected intensity is represented as the incoherent addition of the two domain populations, assuming that each domain has an

identical magnetization magnitude, with directions given by the blue and green curves in Fig. 4(b).

The rotation of the magnetization angle with depth is illustrated in Fig. 4(c) and contrasts that of the constant depth-dependent magnetization angle shown in the inset of Fig. 4(a). It is surprising that, while exchange spring systems are typically bilayers, we observe this behavior in a single film. These results are indicative of magnetic phase segregation in the thin film, where the magnetization is separated into a high coercivity and a low coercivity region. To learn more about the magnetic properties of these regions, the oxygen-deficient sample loop was fit to a combination of two arctangent functions of the form

$$M(H) = A_1 \arctan \frac{H \pm H_{c1}}{w_1} + A_2 \arctan \frac{H \pm H_{c2}}{w_2},$$

where A_i are the amplitudes of the component loops, H_{ci} are the coercivities, and w_i are the broadenings. Here, the index 1 denotes the soft (low coercivity) loop and 2 denotes the hard (large coercivity) component.

The fit to the hysteresis data is shown in Fig. 5(b), revealing a good fit to the model. From the fit, the coercive fields $H_{c1} = 1.32$ mT and $H_{c2} = 26.30$ mT were extracted, indicating that the hard region has an enhanced coercivity of approximately 20 times that of the soft region. The ratio of the amplitudes was determined to be $A_1/A_2 = 28.1 \text{ A m}^{-1}/45.9 \text{ A m}^{-1} = 0.61$. This ratio indicates that the hard magnetic region comprises a significant portion of the sample volume.

The physical origin of this layer is likely related to the localization of OVs at the film-substrate interface. Several studies have indicated that OVs in LSMO as well as other oxides localize near interfaces.^{42–45} The magnetic phase separation indicated by our

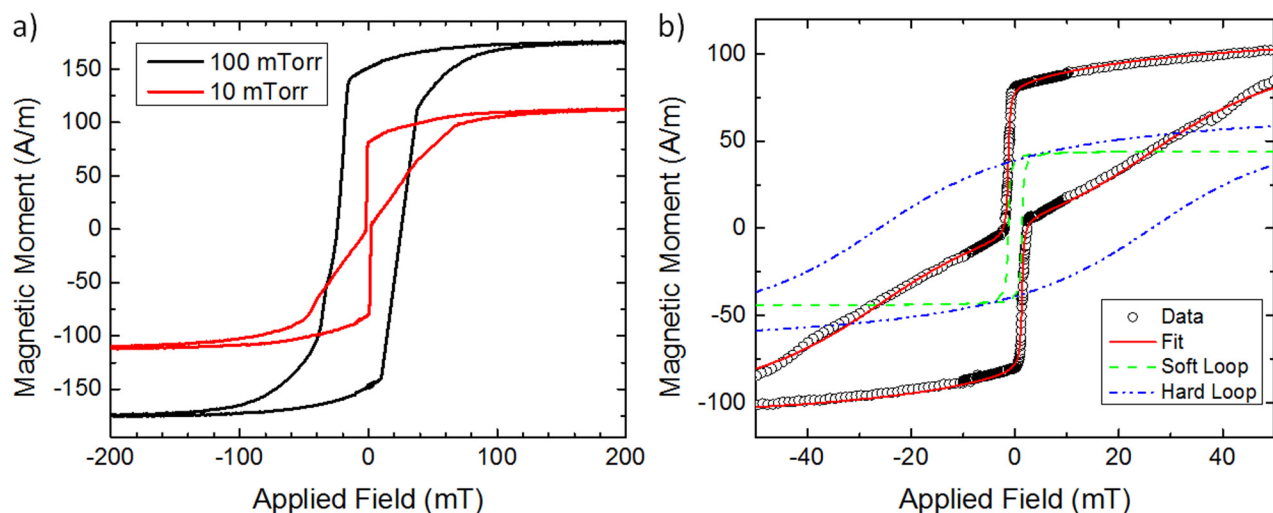


FIG. 5. (a) Magnetic hysteresis loops for the oxygen stoichiometric (100 mTorr, black) and deficient (10 mTorr, red) LSMO films taken at 5 K. (b) Hysteresis loop for the oxygen-deficient sample (open points). The fit is shown as the red solid line, and the dashed lines indicate the component loops extracted from the fits. For both measurements, the magnetic field is applied parallel to the STO (100) direction.

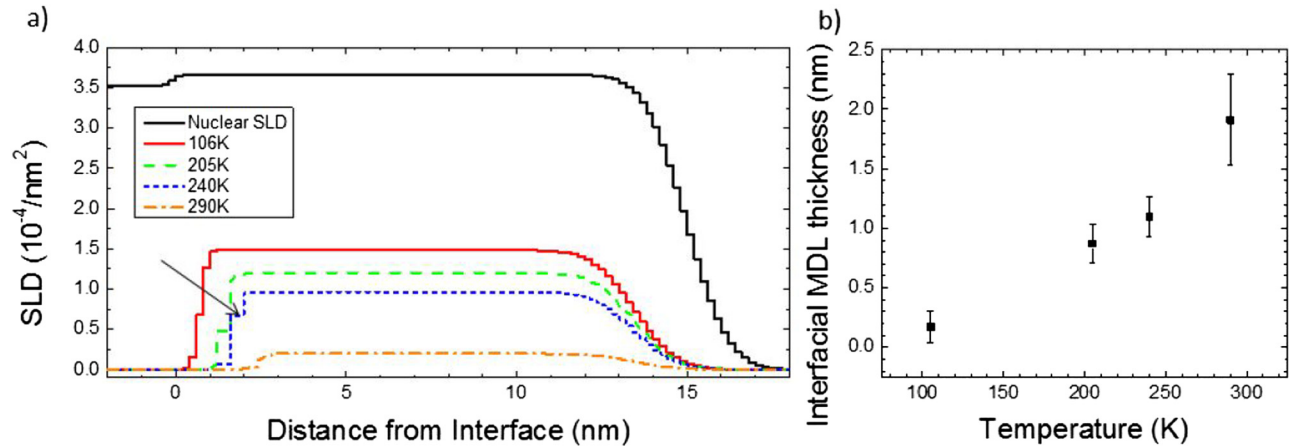


FIG. 6. (a) Temperature dependent magnetic SLD profiles for the oxygen-deficient sample. (b) Temperature dependent thickness of the interfacial magnetic dead layer. Error bars correspond to a range of ± 2 standard deviations as determined from the DREAM fits.

modeling here suggests the presence of an oxygen-deficient region at the interface. The localization of OV's at the interface would result in a region of reduced coercivity relative to the rest of the film. These conclusions are further supported by examining the temperature dependence of the scattering length densities. Figure 6(a) shows the fitted magnetization profile for the oxygen-deficient sample for temperatures of 106 K (above the STO transition), 205, 250, and 290 K. Note that at these temperatures, the exchange spring behavior is lost and the magnetization angle (not shown) is uniform across the whole film.

Comparing the SLDs shown in Figs. 4(a), 4(b), and 6(a), it is evident that while at low temperature neither film shows any evidence of an interfacial dead layer, one begins to form at higher

temperatures in the oxygen-deficient sample. The width of these regions (which are a fit parameter in our modeling) as a function of temperature are shown in Fig. 6(b). The fitting indicates that while the oxygen-deficient sample shows no dead layer at the lowest temperature, the interfacial dead region expands with increasing temperature with a thickness of approximately 1.9 nm obtained near room temperature. The same analysis of the stoichiometric sample indicated no interfacial dead layer across all temperatures (see in the [supplementary material](#), Fig. S4). Note that the surface shows a constant dead layer thickness for all temperatures in both samples, indicating that the surface magnetic dead layer is not solely influenced by oxygen vacancies introduced during growth; however, the contrast in the behavior of the interfacial

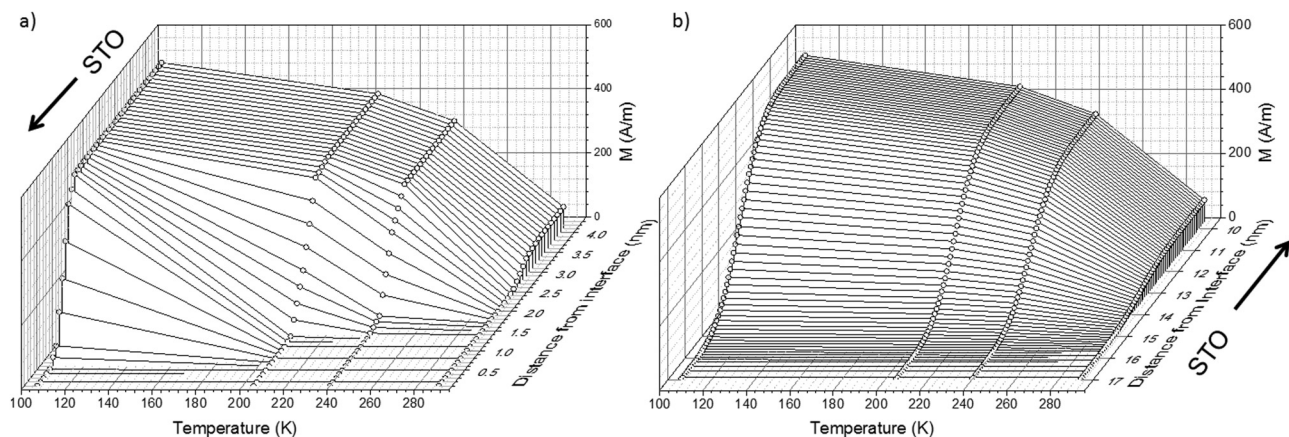


FIG. 7. The Waterfall plot of the temperature dependence of the magnetization within each layer near the (a) LSMO/STO interface and (b) the LSMO surface as a function of distance from the STO interface. The interfacial layers exhibit a reduced critical temperature and changes in features of the temperature dependent magnetization, whereas the surface layers show only a reduction in the magnitude of the magnetization (representing the sigmoidal variation of the magnetization between the film and vacuum in the model). The step size between curves is 0.1 nm. Solid lines are guides to the eye. The direction of the substrate is indicated by arrows.

magnetism of the two films indicates that this behavior likely originates from oxygen vacancies. The increased temperature will also enhance the oxygen mobility, which would lead to a greater number of OV's accumulating at the interface. This leads to a region of deteriorated magnetism which has a lower critical temperature than the rest of the film. Such effects have been observed via PNR for other systems that exhibit a depth-dependent T_c such in compositionally graded $\text{Cu}_x\text{Ni}_{1-x}$ ⁴⁶ and $\text{Co}_{1-x}\text{Ru}_x$ films.⁴⁷

To illustrate this change, line profiles at fixed depths were taken of the four magnetic SLD plots in Fig. 6(a) in order to show the layer by layer temperature dependence of the magnetization. The temperature dependence of the interfacial layers is shown in Fig. 7(a). The majority of the film shows a ferromagneticlike temperature variation except at the interface where the layers begin to show a smeared out transition consistent with the presence of disorder suggested by other studies.^{10–12} Note that this contrasts the depth dependence of the surface magnetization, which shows the same temperature dependence but with reduced magnitude [Fig. 7(b)]. The above results indicate that oxygen vacancies play a significant role in the interfacial magnetism of these thin film systems, leading to a reduction of the Curie temperature with respect to the rest of the film. Similarly, the absence of OV's leads to an enhanced interfacial magnetization.

CONCLUSION

We have determined the magnetization profile of thin film LSMO grown in oxygen-rich and oxygen-poor conditions. The oxygen stoichiometric sample exhibits a strong magnetization at the film-substrate interface and weakened magnetization at the surface, consistent with other reports. The sample shows a negative magnetic moment when measured in ZFC conditions, consistent with our previous results. The moments are rotated approximately 135° from the field parallel direction, corresponding to the STO [110] direction. The depth-dependent results indicate that the sign reversal occurs across the entire film which may point to the formation of an ultrathin interfacial layer of altered magnetic properties which couples to the majority of the film or the interaction of the film's magnetization with an emergent superparamagnetic phase noted in previous studies. The film grown in oxygen-deficient conditions exhibits an overall reduced magnetic moment and a lower relative interfacial magnetization than the oxygen stoichiometric sample. The behavior in ZFC/low field is indicative of a magnetic phase separation leading to exchange spring type behavior. The origin of this behavior is likely related to the localization of OV's at the LSMO/STO interface, which results in a region of reduced ordering temperature and coercivity that couples to the film bulk. These results indicate that the effect of oxygen vacancies on the magnetic properties of these materials is complex and, besides simply reducing the overall film magnetization, can affect the behavior of the magnetic moments in unexpected and nonuniform ways.

SUPPLEMENTARY MATERIAL

See the [supplementary material](#) for AFM characterization of the substrate morphology and termination (Sec. 1), TEM

characterization (Sec. 2), comparison between models for fitting PNR data (Sec. 3), and temperature dependent PNR results (Sec. 4).

ACKNOWLEDGMENTS

Film growth, TEM characterization, and measurement of the oxygen optimized samples were supported by the National Science Foundation (NSF, No. DMR-1608656). Growth and measurement of the oxygen-deficient samples were supported by the U.S. Department of Energy (DOE), Office of Science, Office of Basic Energy Sciences under Award No. DE-SC0016176. We acknowledge the use of the WVU Shared Research Facilities. Certain trade names and company products are identified to specify adequately the experimental procedure. In no case does such identification imply recommendation or endorsement by the National Institute of Standards and Technology, nor does it imply that the products are necessarily the best for the purpose.

REFERENCES

- ¹A.-M. Haghiri-Gosnet and J.-P. Renard, *J. Phys. D Appl. Phys.* **36**, R127 (2003).
- ²M. Angeloni, G. Balestrino, N. G. Boggio, P. G. Medaglia, P. Orgiani, and A. Tebano, *J. Appl. Phys.* **96**(11), 6387 (2004).
- ³L. Marín, L. A. Rodríguez, C. Magén, E. Snoeck, R. Arras, I. Lucas, L. Morellón, P. A. Algarabel, J. M. De Teresa, and M. Ricardo Ibarra, *Nano Lett.* **15**, 492 (2015).
- ⁴A. Tebano, C. Aruta, P. G. Medaglia, F. Tozzi, G. Balestrino, A. A. Sidorenko, G. Allodi, R. De Renzi, G. Ghiringhelli, C. Dallera, L. Braicovich, and N. B. Brookes, *Phys. Rev. B* **74**, 245116 (2006).
- ⁵G. Shibata, K. Yoshimatsu, E. Sakai, V. R. Singh, V. K. Verma, K. Ishigami, T. Harano, T. Kadono, Y. Takeda, T. Okane, Y. Saitoh, H. Yamagami, A. Sawa, H. Kumigashira, M. Oshima, T. Koide, and A. Fujimori, *Phys. Rev. B* **89**, 235123 (2014).
- ⁶K. Oguz, P. Jivrajka, M. Venkatesan, G. Feng, and J. M. D. Coey, *J. Appl. Phys.* **103**(7), 07B526 (2008).
- ⁷Z. Li, M. Bosman, Z. Yang, P. Ren, L. Wang, L. Cao, X. Yu, C. Ke, M. B. H. Breese, A. Rusydi, W. Zhu, Z. Dong, and Y. L. Foo, *Adv. Func. Mater.* **22**, 4312 (2012).
- ⁸N. Mottaghi, M. S. Seehra, R. Trappen, S. Kumari, C.-Y. Huang, S. Yousefi, G. B. Cabrera, A. H. Romero, and M. B. Holcomb, *AIP Adv.* **8**, 056319 (2018).
- ⁹N. Mottaghi, R. B. Trappen, S. Kumari, C.-Y. Huang, S. Yousefi, G. B. Cabrera, M. Aziziha, A. Haertter, M. B. Johnson, M. S. Seehra, and M. B. Holcomb, *J. Phys. Condens. Matter* **30**, 405804 (2018).
- ¹⁰B. Cui, C. Song, F. Li, G. Y. Wang, H. J. Mao, J. J. Peng, F. Zeng, and F. Pan, *Sci. Rep.* **4**, 4206 (2015).
- ¹¹H. Guo, J.-O. Wang, X. He, Z. Yang, Q. Zhang, K.-J. Jin, C. Ge, R. Zhao, L. Gu, Y. Feng, W. Zhou, X. Li, Q. Wan, M. He, C. Hong, Z. Guo, C. Wang, H. Lu, K. Ibrahim, S. Meng, H. Yang, and G. Yang, *Adv. Mater. Interfaces* **3**, 1500753 (2016).
- ¹²J. Sakai, N. Ito, and S. Imai, *J. Appl. Phys.* **99**, 08Q318 (2006).
- ¹³D. A. Gilbert, A. J. Grutter, E. Arenholz, K. Liu, B. J. Kirby, J. A. Borchers, and B. B. Maranville, *Nat. Commun.* **7**, 12264 (2016).
- ¹⁴A. J. Grutter, D. A. Gilbert, U. S. Alaán, E. Arenholz, B. B. Maranville, J. A. Borchers, Y. Suzuki, K. Liu, and B. J. Kirby, *Appl. Phys. Lett.* **108**, 082405 (2016).
- ¹⁵H. Boschker, M. Huijben, A. Vailionis, J. Verbeeck, S. van Aert, M. Luysberg, S. Bals, G. van Tendeloo, E. P. Houwman, G. Koster, D. H. A. Blank, and G. Rijnders, *J. Phys. D Appl. Phys.* **44**, 205001 (2011).
- ¹⁶J. G. Connell, B. J. Isaac, G. B. Ekanayake, D. R. Strachan, and S. S. A. Seom, *Appl. Phys. Lett.* **101**, 251607 (2012).
- ¹⁷M. Björch and G. Andersson, *J. Appl. Crystallogr.* **40**, 1174 (2007).

- ¹⁸R. Trappen, A. C. Garcia-Castro, V. T. Tra, C.-Y. Huang, W. Ibarra-Hernandez, J. Fitch, S. Singh, J. Zhou, G. Cabrera, Y.-H. Chu, J. M. LeBeau, A. H. Romero, and M. B. Holcomb, *Sci. Rep.* **8**, 14313 (2018).
- ¹⁹S. J. Blundell and J. A. C. Bland, *Phys. Rev. B* **46**(6), 3391 (1992).
- ²⁰P. A. Kienzie, B. B. Maranville, K. V. O'Donovan, J. F. Ankner, N. F. Berk, C. F. Majkrzak, see <https://www.nist.gov/ncnr/reflectometry-software> for information on ReFlID as well as a download link (2017).
- ²¹J. A. Vrugt, C. J. F. ter Braak, C. G. H. Diks, B. A. Robinson, J. M. Hyman, and D. Higdon, *Int. J. Nonlinear Sci. Numer. Simul.* **10**(3), 273 (2009).
- ²²E.-J. Guo, T. Charlton, H. Ambaye, R. D. Desautels, H. N. Lee, and M. R. Fitzsimmons, *ACS Appl. Mater. Interfaces* **9**, 19307 (2017).
- ²³S. Singh, T.-Y. Chien, J. R. Guest, and M. R. Fitzsimmons, *Phys. Rev. B* **85**, 115450 (2012).
- ²⁴S. Saha, O. Kahya, M. Jaiswal, A. Srivastava, A. Annadi, J. Balakrishnan, A. Pachoud, C.-T. Toh, B.-H. Hong, J.-H. Ahn, T. Venkatesan, and B. Özyilmaz, *Sci. Rep.* **4**, 6173 (2015).
- ²⁵S. Yousefi, S. Singh, A. C. Garcia-Castro, R. Trappen, G. B. Cabrera, N. Mottaghi, C.-Y. Huang, S. Kumari, G. Bhandari, A. D. Bristow, A. H. Romero, and M. B. Holcomb, *ACS Nano* **13**(3), 3457 (2019).
- ²⁶T. T. Fister, D. D. Fong, J. A. Eastman, P. M. Baldo, M. J. Highland, P. H. Fuoss, K. R. Balasubramaniam, J. C. Meador, and P. A. Salvador, *Appl. Phys. Lett.* **93**, 151904 (2008).
- ²⁷W. Lee, J. W. Han, Y. Chen, Z. Cai, and B. Yildiz, *J. Am. Chem. Soc.* **135**, 7909 (2013).
- ²⁸F. Ott, M. Viret, R. Borges, R. Lyonnet, E. Jacquet, C. Fermon, and J.-P. Contour, *J. Magn. Magn. Mater.* **211**, 200 (2000).
- ²⁹E. J. Moon, P. V. Balachandran, B. J. Kirby, D. J. Keavney, R. J. Sichel-Tissot, C. M. Sclepütz, E. Karapetrova, X. M. Cheng, J. M. Rondinelli, and S. J. May, *Nano Lett.* **14**, 2509 (2014).
- ³⁰M. Saghayezhia, S. Kouser, Z. Wang, H. Guo, R. Jin, J. Zhang, Y. Shu, S. T. Pantelides, and E. W. Plummer, *Proc. Natl. Acad. Sci. U.S.A.* **116**, 201819570 (2019).
- ³¹J.-S. Lee, D. A. Arena, P. Yu, C. S. Nelson, R. Fan, C. J. Kinane, S. Langridge, M. D. Rossell, R. Ramesh, and C.-C. Kao, *Phys. Rev. Lett.* **105**, 257204 (2010).
- ³²J.-S. Lee, C.-C. Kao, T. S. Santos, E. Negusse, and D. A. Arena, *J. Phys. D Appl. Phys.* **44**(24), 245002 (2011).
- ³³M. Mathews, F. M. Postma, J. Cock Lodder, R. Jansen, G. Rijnders, and D. H. A. Blank, *Appl. Phys. Lett.* **87**, 242507 (2005).
- ³⁴S. Gu, W. He, M. Zhang, T. Zhuang, Y. Jin, H. ElBidweihy, Y. Mao, J. H. Dickerson, M. J. Wagner, E. D. Torre, and L. H. Bennett, *Sci. Rep.* **4**, 6267 (2014).
- ³⁵L. Fallarino, B. J. Kirby, M. Pancaldi, P. Riego, A. L. Balk, C. W. Miller, P. Vavassori, and A. Berger, *Phys. Rev. B* **95**, 134445 (2017).
- ³⁶E. F. Kneller, *IEEE Trans. Magn.* **27**(4), 3588 (1991).
- ³⁷O. de Abril and M. del Carmen Sánchez, *J. Appl. Phys.* **100**, 063904 (2006).
- ³⁸M. A. Moskalenko, V. M. Uzdin, and H. Zabel, *J. Appl. Phys.* **115**, 053913 (2014).
- ³⁹B. Li, R. V. Chopdekar, E. Arenholz, A. Mehta, and Y. Takamura, *Appl. Phys. Lett.* **105**, 202401 (2014).
- ⁴⁰D. J. Dunlop, *Rep. Prog. Phys.* **53**, 707 (1990).
- ⁴¹L. Tauxe, H. N. Bertram, and C. Seberino, *Geochim. Geophys.* **3**(10), 1 (2002).
- ⁴²K. Hirai, R. Aso, Y. Ozaki, D. Kan, M. Haruta, N. Ichikawa, H. Kurata, and Y. Shimakawa, *ACS Appl. Mater. Interfaces* **9**, 30143 (2017).
- ⁴³M. Nord, P. E. Vullum, M. Moreau, J. E. Boschker, S. M. Selback, R. Holmestad, and T. Tybell, *Appl. Phys. Lett.* **106**, 041604 (2015).
- ⁴⁴K. H. L. Zhang, G. Li, S. R. Spurgeon, L. Wang, P. Yan, Z. Wang, M. Gu, T. Varga, M. E. Bowden, Z. Zhu, C. Wang, and Y. Du, *ACS Appl. Mater. Interfaces* **10**, 17480 (2018).
- ⁴⁵T. L. Meyer, A. Herkoltz, V. Lauter, J. W. Freeland, J. Nichols, E.-J. Guo, S. Lee, T. Z. Ward, N. Balke, S. V. Kalinin, M. R. Fitzsimmons, and H. N. Lee, *Adv. Electron. Mater.* **2**, 1500201 (2016).
- ⁴⁶B. J. Kirby, H. F. Belliveau, D. D. Belyea, P. A. Kienzie, A. J. Grutter, P. Riego, A. Berger, and C. W. Miller, *Phys. Rev. Lett.* **116**, 047203 (2016).
- ⁴⁷B. J. Kirby, L. Fallarino, P. Riego, B. B. Maranville, C. W. Miller, and A. Berger, *Phys. Rev. B* **98**, 064404 (2018).